On-Site Non-Invasive Current Monitoring of Multi-Core Underground Power Cables With a Magnetic-Field Sensing Platform at a Substation

Ke Zhu, *Student Member, IEEE*, Wei Han, *Student Member, IEEE*, Wing Kin Lee, and Philip W. T. Pong, *Senior Member, IEEE*

***Abstract*— Current monitoring can facilitate preemptive action in electrical distribution network, so as to relieve power congestion, improve transmission efficiency, and ensure network reliability. The non-invasive current sensing devices are promising since they do not require contacting hazardous high voltage and their installation is much easier compared with invasive current sensing devices. However, the existing non-invasive current sensing devices, such as current clamps and Rogowski coils are only applicable for measuring single-core underground power cables. In this paper, we established a non-invasive technique, that can monitor the currents of a multi-core underground power cable by measuring the emitted magnetic field around the cable surface. The additional magnetic fields generated by induced and leakage currents on the cables were firstly evaluated. Magnetoresistive (MR) sensors in a circular array were adopted to measure magnetic field around the cable surface, and a triple-layer shielding was designed to reduce the effects of external interference. Regarding intrinsic noise in MR sensors (e.g., 1/f noise and thermal noise), magnetic flux concentrators were supplemented to improve the signal-to-noise ratio. The developed platform was tested in a substation, and the reconstructed results closely matched the real geometrical configuration and current records of the tested cable. Apart from the non-invasive feature, the platform also shows great potential to improve the sensing capability of current amplitude and frequency compared with CTs by adopting MR sensors.**

***Index Terms*— Current monitoring, magnetic-field sensing, underground power cable.**

I. Introduction

IN METROPOLITAN areas, underground power cables are more commonly deployed than aerial transmission lines because of reduced environmental impact, lower emanated magnetic fields, less transmission loss, and better voltage regulation [1], [2]. The demand for electric power has grown significantly faster than the expansion of underground transmission grids, however, leading to a shortage of transmission capacity and more disturbances [3]. Power flow through underground power cables has become more dynamic as a consequence of growing exploitation of renewable energy [4] and nonlinear power electronic loads [5], such as those related to induction and spark furnaces in urban plants. Real-time current monitoring of underground power cables enables engineers to take timely control measures to relieve congestion, facilitate safe power transmission, and improve network reliability. Moreover, the accurate and swift detection of short-circuit faults is especially critical to isolate the system for minimizing the damage to equipment, and the risk of fire or injury of the personnel. In short, current monitoring of underground power cables plays a significant role in power transmission and distribution for metropolitans [6].

Invasive current sensing devices (e.g., CTs, shunt resistors) are widely used in the power systems [7]–[9]. Unluckily, due to the unavoidable physical connection with the primary circuit, there are a series of problems [9]. Firstly, since the invasive devices contact with the high voltage of the primary circuit, they need to be very well insulated in order to avoid short-circuit fault of the primary circuit due to high-voltage arc discharging, and also to eliminate the risk of electric shock. Secondly, the installation of the devices can be complicated since the primary circuits should be opened and interrupted to install them. Due to these shortcomings, the invasive devices tend to be bulky (e.g., volume size of CT is in the order of m^3 [10]), expensive (e.g., CT typically costs over US$ 100k [11]) and difficult to be installed. Thus they are infeasible for deployment beyond substations in a wide area for enhancing situation awareness in the Smart Grid construction [12]. They are also not applicable for serviceman to implement on-site work. As such, the non-invasive current sensing devices are more promising to be further developed in power systems since they do not come across the mentioned problems [13]–[16]. Their installation is much simpler and safer because there is no complication of opening and contacting the primary high-voltage circuit and thus no risk of electric shock. Since these sensing devices are not directly in touch with the high-voltage parts, they do not need insulation which reduces the size and cost. Therefore, they are more suitable to be deployed largely in a wide area

Manuscript received November 28, 2016; revised January 9, 2017; accepted January 10, 2017. Date of publication January 11, 2017; date of current version February 17, 2017. This work was supported in part by the Seed Funding Program for Basic Research and Small Project Funding Program from the University of Hong Kong, ITF Tier 3 Funding under Grant ITS/214/14 and in part by the University Grants Committee of Hong Kong under Contract AoE/P-04/08. This is an expanded paper from the IEEE SENSORS 2015 Conference. The associate editor coordinating the review of this paper and approving it for publication was Prof. Tarikul Islam. *(Corresponding author: Philip W. T. Pong.)*

The authors are with the Department of Electrical and Electronic Engineering, University of Hong Kong, Hong Kong (e-mail: zhuke@hku.hk; weihan@eee.hku.hk; wklee@eee.hku.hk; ppong@eee.hku.hk).

Digital Object Identifier 10.1109/JSEN.2017.2651886

for situational awareness of the whole power system and to be equipped by the serviceman for portable use. However, the existing non-invasive current sensing devices such as current clamps and Rogowski coils [17], [18] are only applicable for measuring single-core underground power cables; they are not applicable for multi-core underground power cables since they measure the overall net magnetic field around the conductor [19]. If a three-phase three-core power cable with balanced currents is clamped, these devices would indicate a reading of zero. The only way to do it is to remove the insulating layers of the multi-core underground power cable so that the conductors are exposed to be clamped individually by current clamps or Rogowski coils [2], [20]. In order to overcome such limitation and inconvenience, it is very useful to develop a non-invasive platform for measuring the currents of the multi-core underground power cable.

In a previous study, we proposed a non-invasive technique for reconstructing the current of the multi-core power cable from the emitted magnetic fields [21]. The magnetic fields do not terminate like electric fields on the earthed metallic sheath, but are still detectable around the cable surface [2], [21], [22]. The three-phase currents were reconstructed by processing the measured magnetic fields around the cable surface by a stochastic optimization algorithm. However, there are several remaining practical problems to be solved before this technique can be put into practice as a real platform. Firstly, apart from the loading currents, the induced and leakage currents also exist on the underground power cables which can generate the additional magnetic fields [23]. Secondly, there are background magnetic fields such as those from the Earth and other current sources (e.g. other neighboring underground power cables) which are irrelevant to the current sources. Last but not least, intrinsic noise in MR sensors (e.g., 1/f noise) [24] can also influence the accuracy of magnetic field measurement. Increasing the signal-to-noise ratio, to this effect, is an important aspect of continuing research.

In this paper, we developed and implemented a platform that can carry out non-invasive current monitoring of underground power cables based on sensing magnetic fields around the cable surface. The analytical model was constructed in advance to evaluate the induced current due to neighboring cables by taking two adjacent BS6622 three-phase three-core armored 22 kV XLPE stranded underground power cables as an example. By analyzing different conditions of the adjacent cable regarding its length, relative position, and rated current, the amplitude and influence of induced currents were analyzed in detail. Meanwhile, the effects of the leakage currents were evaluated. A triple-layer magnetic shielding was carefully designed and fabricated to eliminate background magnetic interference. A set of curved-trapezoidal magnetic flux concentrators were also integrated to improve the signal-to-noise ratio. The on-site test was conducted for a three-phase three-core armored 22 kV XLPE stranded underground power cable in a sub-station. These power cables are typically buried underground in the city, while they are housed in the cable room of the sub-station and are accessible above ground level. Therefore, in our work, the experiment for the three-phase power cable was conducted at the sub-station to avoid the excavation work. During the on-site experiment, the magnetic fields around the cable were measured and then processed by the stochastic optimization algorithm to reconstruct the electrical and geometrical parameters successfully. This non-invasive platform shows a great potential to improve sensing capability on current amplitude and frequency compared to CTs by deploying MR sensors.

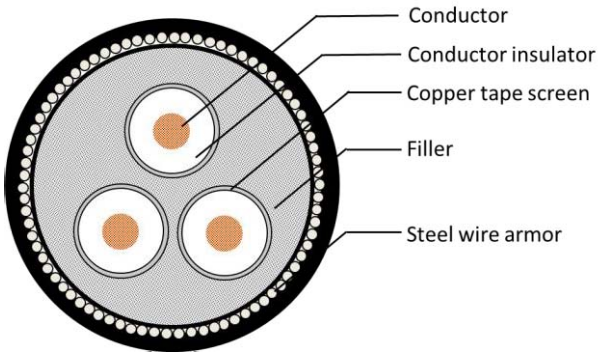

Fig. 1. Structure of the three-phase armored 22 kV XLPE stranded underground cable. Radius: (1) conductor, 10 mm; (2) copper tape screen, 15 mm (inner) and 16 mm (outer); (3) steel wire armor: 40 mm (inner) and 42 mm (outer).

II. Magnetic-Field Sensing for Reconstructing Currents of Underground Power Cable

A. Magnetic Flux Density Around Cable Surface

The magnitude and pattern of magnetic fields around the cable surface can be attained by the finite element method (FEM). The FEM approach is taken rather than using the analytical approach so that this method can be easily adapted to cables with other geometrical and material parameters. In this study, the platform design and on-site test were based on a three-phase three-core armored 22 kV XLPE stranded underground power cable [25], whose structure and material are shown in Fig. 1. The three-phase conductors were surrounded by copper tape screens, and the steel wire armor was grounded at both ends to ensure safety and reliable operation. The phase conductors are insulated by conductor insulators and fillers. The electromagnetic characteristic of each component is described by the relative permeability ($\boldsymbol{\mu_r}$), relative permittivity ($\boldsymbol{\epsilon_r}$), and conductivity ($\boldsymbol{\sigma_r}$) and as listed in Table. I. The FEM results for the magnetic fields around the cable surface was shown in Fig. 2(a), and the details are addressed as following:

1) Magnitude of Magnetic Fields: The magnitude of the magnetic flux density around the cable surface was about 10 mG regarding a rated phase current of 1 A. Typically, the magnitude of loading currents are generally from tens to hundreds of amperes for underground power cables [26]. As such, the RMS magnetic flux density around the cable surface would be hundreds of mG when the loading currents of underground power cables are tens of amperes, or to the extent of thousands of mG at current magnitudes of hundreds of amperes [27]. These magnetic fields are well within the

TABLE I
ELECTROMAGNETIC PROPERTY OF THREE-PHASE ARMORED 22 KV XLPE UNDERGROUND POWER CABLE

Element	μ_r	ϵ_r	σ_r (s/m)
Conductor	1.0	1.0	5.8×10^7
XLPE conductor insulator	1.0	2.3	0.0
Copper tape screen	1.0	1.0	5.8×10^7
Polypropylene filler	1.0	2.3	0.0
Steel wire armor	40	1.0	1.1×10^7

detection range of MR sensors whose upper limit can be as high as tens of gauss [16].

2) Direction of Magnetic Fields: The magnetic flux lines are no longer symmetrically circular but exhibit an oval pattern around the cable surface regarding the cable center. Namely, the vector of the resultant magnetic field (B_s) around the multi-core cable surface in a circle at various points are not necessarily tangential, but indeed forms different angles with regard to the cable center. Therefore, the MR sensors with mutually orthogonal sensing axes in a plane (B_x and B_y) are needed for reconstituting the resultant magnetic field (B_s).

3) Pattern of Magnetic Fields: The proposed method for reconstructing the three-phase currents is based on the measurement of magnetic field distribution around the cable surface. The RMS magnetic field distribution as a function of azimuths (θ) around the cable surface (radius is R shown in Fig. 2(a)) under balanced condition is shown in Fig. 2(b). The magnetic field exhibits a repeated peak and trough at a period of $2\pi/3$, and the strongest magnetic fields are measured where the sensing points are nearby the phase conductors due to a closer distance to the phase conductor (i.e., three peaks). The phase currents are calculated by an iterative inverse algorithm with stochastic optimization to minimize the Euclidean difference between the calculated and the measured magnetic field distribution. The three-phase currents can be reconstructed based on the measured magnetic field distribution in our technique whereas the current clamps or the Rogowski coils would give a reading of almost zero if they clamp around a cable with three-phase balanced currents.

4) Location of MR Sensors: Since the magnitude of the magnetic field is inversely proportional to the distance of its second power as indicated by Biot-savart law, the magnitude of magnetic flux density drops when the sensing points are gradually farther away. The magnitude of the resultant magnetic flux density as a function of horizontal displacement of sensing point (x in Fig. 2(a)) by FEM is shown in Fig. 2(c), exhibiting that the magnitude decays when the sensing points move away from the cable surface. For our technique, the MR sensors are located around the cable surface and they are close to the current sources, so the magnetic signal is still strong for measurement.

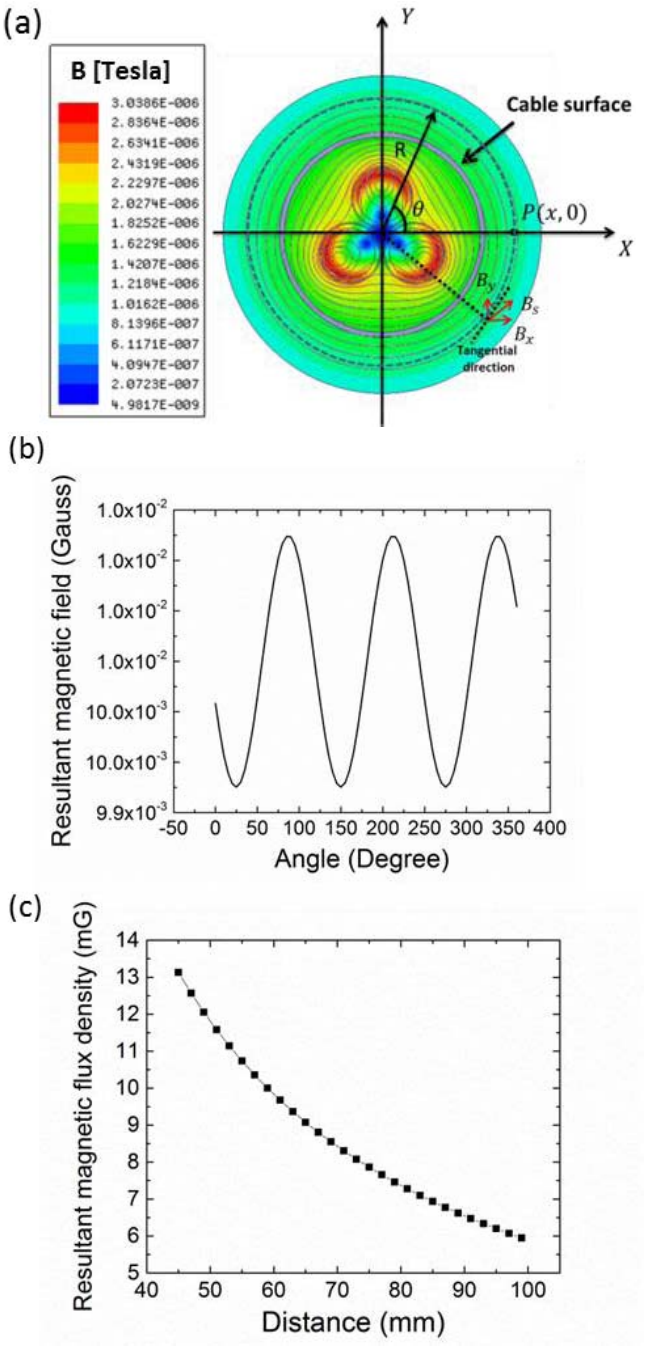

Fig. 2. Magnetic field around the cable surface. (a) Magnetic fields around the cable surface in FEM simulation. (b) Magnitude of the resultant magnetic fields in a circle as a function of azimuth (R=60 mm). (c) Resultant magnetic flux density as a function of horizontal displacement $P(x, 0)$.

B. Leakage and Induced Current Impact

Apart from the loading currents flowing on the phase conductors, leakage and induce currents also exist on the underground power cables [2], [28]. The XLPE layers can be damaged by water treeing and electrical treeing, leading to the leakage current flowing from the phase conductor to the sheath. The leakage currents of underground power cables are generally in the level of μA [29]–[32], which are extremely small compared to the magnitude of loading currents (tens to hundreds of amperes). Therefore, the magnetic fields generated

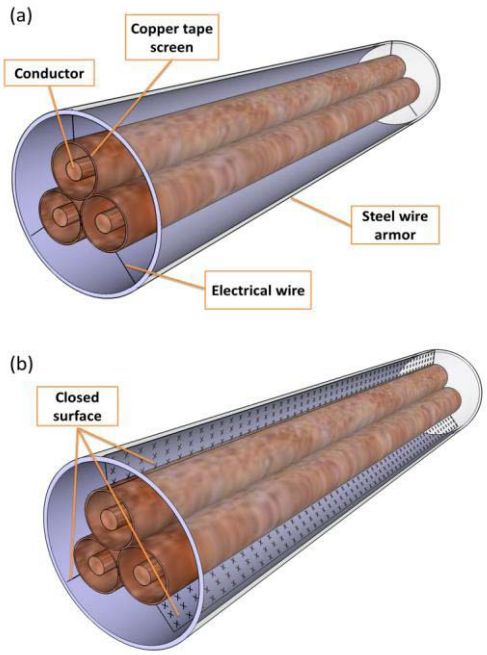

Fig. 3. Three-phase three-core armored 22 kV XLPE stranded underground power cable. (a) Structure and radius of each component: (1) conductor (copper), 10 mm; (2) copper tape screen, 15 mm (inner) and 16 mm (outer); (3) steel wire armor: 40 mm (inner) and 42 mm (outer). (b) Closed surface where the magnetic flux passes through.

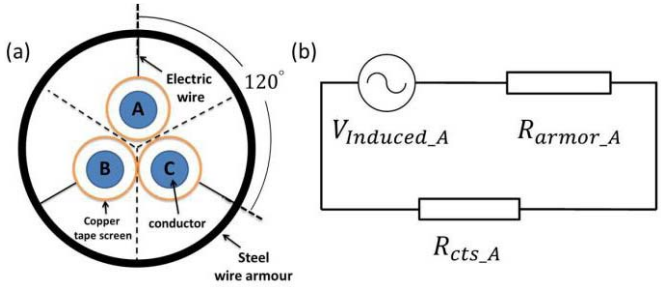

Fig. 4. Induced voltage model. (a) Cross section of underground cable divided into three equivalent parts. (b) Electric circuit composed of induced voltage and resistors (steel wire armor and copper tape screen).

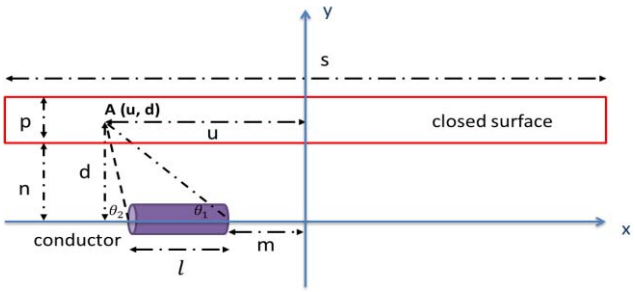

Fig. 5. Magnetic flux density at a point generated from a single adjacent current-carrying conductor.

by the leakage currents are ignorable compared to those from the loading currents.

The induced current on the target multi-core underground power cable needs to be evaluated. Though the electric fields from the power cables are heavily shielded by copper layers and steel wire armor, the magnetic fields cannot be shielded since copper and steel are not materials of high permeability. Moreover, underground power cables are typically placed closely to each other and thus they can be coupled by the alternating magnetic fields. Therefore, the induced voltage on the target multi-core underground power cable should be evaluated. Based on Faraday's law of induction, the induced electromotive force in any closed circuit is equal to the rate of change of the magnetic flux enclosed by the circuit. Mathematically, it is expressed as

$$\varepsilon = -\frac{d\Phi_B}{dt} \tag{1}$$

where ε is the electromotive force (EMF), and Φ_B is the magnetic flux. Induced current is incurred if the circuit is closed. Regarding the nature of three-phase underground power cable configurations, each screen of phase conductor and the armor are earthed in principle so as to divert any fault current to the ground in the fault conditions. Accordingly, the closed circuit is formed between the screen of the phase conductor and the armor of the underground power cable, and the induced currents thus appear where there are induced voltages. The structure of the target cable is depicted in Fig. 3(a). Each copper conductor is surrounded by a thin copper tape screen, and the steel wire armor is connected with each of these screens at each end of the cable. Under this setup, the closed surface is formed of each phase where an induced voltage would be incurred when the changing magnetic flux pass through (Fig. 3(b)). The induced current flows through the closed circuit composed of the steel wire armor, copper tape screen and the electrical wires.

For simplicity, the underground power cable is assumed to be homogenous, and thus the cross section of the cable can be symmetrically divided into three equivalent sections corresponding to three phases (Fig. 4(a)). The equivalent electric circuit model for studying the induced current is shown in Fig. 4(b), where phase A serves as an example. The resistance is proportional to its electrical resistivity and length, and is inversely proportional to the cross-sectional area. As such, the resistance of the copper tape screen (R_{cts_A}) and the armor (R_{armor_A}) with respect to phase A can be calculated as

$$R_{cts\_A} = \rho_{cts}\frac{s}{\pi\,(2r_{cts} - t_s)\,t_s} \tag{2}$$

$$R_{armor\_A} = \rho_{armor}\frac{s}{\frac{\pi\,(2r_a - t_a)t_a}{3}} \tag{3}$$

where s is the length of target cable, ρ_{armor}, ρ_{cts} are the resistivity of steel wire armor and copper tape screen respectively, r_a, r_{cts} are the outer radius of armor and copper tape screen respectively, and t_s , t_a are the thickness of armor and copper tape screen respectively.

In order to calculate the induced voltage on the target multi-core underground power cable affected by an adjacent one, the induced voltage of a closed surface near a single conductor is calculated first (Fig. 5). The closed surface denotes the closed circuit composed of the steel wire armor, copper tape screen and the electrical wires (see Fig. 3). The magnetic field ($B(u, d)$) at a point ($A(u, d)$) within the surface

generated from the single conductor is calculated by Eq. (4), as shown at the bottom of this page, where μ_0 is the magnetic constant, I is the magnitude of the current on the conductor, and the other spatial parameters are denoted in Fig. 5. The magnetic flux through the surface (Φ_B) is then calculated as the surface integral of the magnetic field passing through. Then the induced voltage indicated by Eq. (1) is calculated as (5), shown at the bottom of this page, where f is frequency of conductor current, p is the width of the closed surface, and s is the length of the closed surface. Based on this result, the induced voltage on the multi-core power cables can be derived. In Fig. 6(a), the induced voltage of a three-phase underground power cable is modeled with an adjacent same-type cable in service. The alternating magnetic fields emitted from each of the phase conductors of this adjacent three-phase cable pass through the closed surface of the phase A of the target cable. When conducting a sinusoidal current of amplitude I and frequency f, the voltage induced in the closed surface by phase A of the adjacent cable is calculated by (6), shown at the bottom of this page, where the width of the closed surface is p, the distance between the closed surface (phase A) of the target cable and the center of the conductor (phase A) of the adjacent cable is n, the length of the target cable (adjacent cable) is $s(l)$, and the distance betwen the central axis of the target cable and the tail end of the adjacent cable is m. The magnetic fields emitted from the other two phases forms an angle with the closed surface. For example, the voltage induced by phase B of the adjacent cable (Fig. 6(b)) is calculated by (7) and (8), where d_B is the distance from the closed surface to the conductor center of phase B of the adjacent cable, r is the distance between each phase conductor center to the center of the adjacent cable, and θ_B is defined in the Fig. 6(b). The induced voltage by phase C of the adjacent cable is calculated similarly via (7) and (8). As such, the induced voltage on phase A of the target cable is the total contribution of the induced voltages incurred by the three-phase currents of the adjacent cable.

The peak value of the induced current on phase A of the target cable is calculated under various lengths, relative positions, and rated currents of the adjacent three-phase cable (Fig. 7). The results show that the amplitude of induced current is very weak whose value is only several tenths of an ampere. Compared to the typical load current for underground power cables ranging from tens to hundreds of amperes [25],

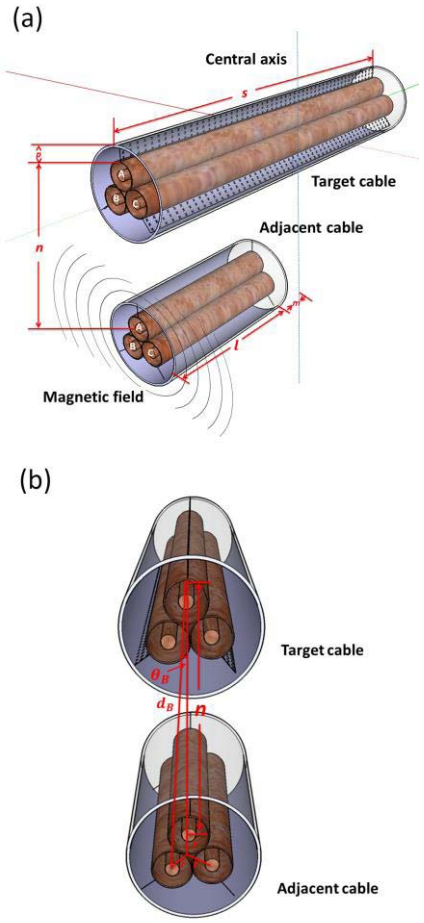

Fig. 6. Layout of target and adjacent three-phase underground power cables for calculating induced voltage on a phase conductor (phase A in this case) of the target underground power cable. (a) Side view. (b) Front view.

$$B(u,d)=\frac{\mu_o I}{4\pi d}(\cos\theta_1-\cos\theta_2)=\frac{\mu_o I}{4\pi d}\left(\frac{u-m}{\sqrt{(u-m)^2+d^2}}-\frac{u-l-m}{\sqrt{(u-l-m)^2+d^2}}\right) \tag{4}$$

$$V(t)=\mu_o sfI\cos(2\pi ft)*ln\frac{n+p}{n}*\left(\frac{(l+m)}{\sqrt{\left(\frac{s}{2}-l-m\right)^2+n^2}+\sqrt{\left(\frac{s}{2}+l+m\right)^2+n^2}}-\frac{m}{\sqrt{\left(\frac{s}{2}-m\right)^2+n^2}+\sqrt{\left(\frac{s}{2}+m\right)^2+n^2}}\right) \tag{5}$$

$$V_1(t)=\mu_o sfI\cos(2\pi ft)*ln\frac{n+p}{n}*\left(\frac{l+m}{\sqrt{\left(\frac{s}{2}-l-m\right)^2+n^2}+\sqrt{\left(\frac{s}{2}+l+m\right)^2+n^2}}-\frac{m}{\sqrt{\left(\frac{s}{2}-m\right)^2+n^2}+\sqrt{\left(\frac{s}{2}+m\right)^2+n^2}}\right) \tag{6}$$

$$V_2(t)=\mu_o sfI\cos(2\pi ft+\varphi_B)*ln\frac{d_B+p}{d_B}*\left(\frac{l+m}{\sqrt{\left(\frac{s}{2}-l-m\right)^2+d_B^2}+\sqrt{\left(\frac{s}{2}+l+m\right)^2+d_B^2}}-\frac{m}{\sqrt{\left(\frac{s}{2}-m\right)^2+d_B^2}+\sqrt{\left(\frac{s}{2}+m\right)^2+d_B^2}}\right)*\cos\theta_B \tag{7}$$

$$r^2=d_B^2+(n+r)^2-2d_B(n+r)\cos\theta_B \tag{8}$$

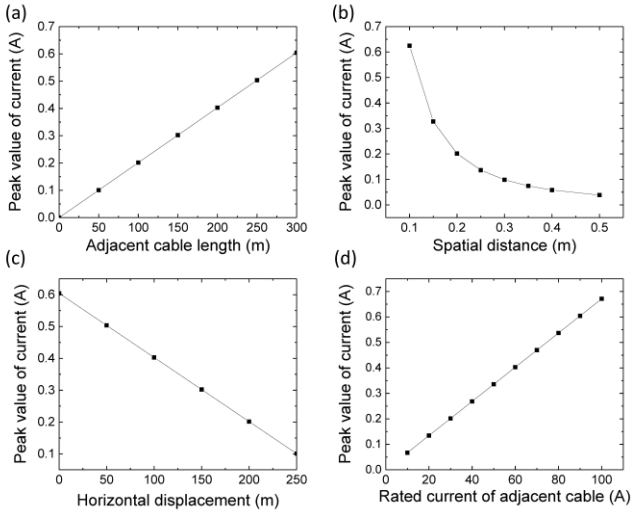

Fig. 7. Induced current calculation on a 600 m underground cable with different configuration of adjacent cable. (a) Adjacent cable length (l) changes from 0 to 300 m ($n = 0.2$ m, $m = 0$ m, $I = 30$ A). (b) Distance between target and adjacent cable (n) changes from 0.1 to 0.5 m ($l = 100$ m, $m = 0$ m, $I = 30$ A). (c) Position of adjacent cable (m) changes from 0 to 250 m ($l = 300$ m, $n = 0.1$ m, $I = 30$ A). Rated current (I) changes from 10 to 100 A ($l = 100$ m, $n = 0.2$ m, $m = 0$ m).

the effect of the induced current is very limited. Based on this fact, magnetic fields around the cable surface emitted by induced current are insignificant compared to load currents. Therefore, the magnetic flux density measured around cable surface can be used directly for the subsequent current reconstruction process, in which way the reconstructed currents should have a high accuracy.

C. Stochastic Program for Current Reconstruction

Based on the Biot-Savart law, the magnitude and distribution of magnetic fields are related to the positions and currents of the conductors. The reconstruction from the magnetic fields to the current sources is a multi-variable inverse problem. The current cannot be reconstructed from the magnetic fields analytically easily as the conductor positions of underground power cables are unknown. Here, we utilize a stochastic algorithm to reconstruct the geometrical configuration and current status of the underground power cable from the measured magnetic field information.

From Biot-Savart law, the magnetic field is related to both the magnitude and positions of the currents. In the program (Fig. 8), the optimization is operated on both the phase currents and the positions of the conductors. The components of the algorithm are inverse current program (ICP), magnetic field evaluation (MFE) and source position optimization (SPO). The ICP commences with a default setup of three-phase conductor position P_o and the measured magnetic flux density B_{mea}. The geometrical profile of the target cable is known, and thus the default positions of the cable can be set as reasonable initial values. The phase currents are optimized by finding the minimum of the objection function

$$f = ||AI_p - B_{mea}|| \tag{9}$$

which gives rise to

$$I_p = (A^T A)^{-1} A^T B_{mea} \tag{10}$$

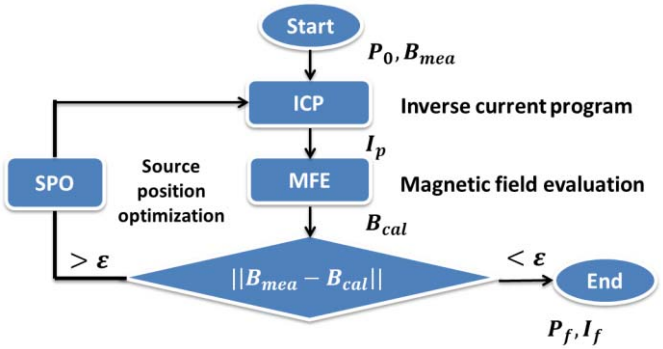

Fig. 8. Program to reconstruct positions and currents of a three-phase three-core underground power cable.

where A is a coefficient matrix that depends on the current sources of the three-phase three-core underground power cable [21]. Then magnetic field B_{cal} is calculated via finite element method in the MFE module with updated current values I_p. If the Euclidian distance between B_{cal} and B_{mea} is smaller than the pre-set threshold (ε), the algorithm will terminate and output the reconstructed three-phase conductor position P_f and current information I_f; otherwise, the conductor positions are optimized by SPO module via artificial immune system (AIS) [33], [34]. With generated conductor positions, I_p will be updated in ICP again. The iteration continues until the Euclidian distance condition is achieved, and the final I_p is obtained as the currents of the conductors. More details regarding this reconstruction process can be found in [21].

III. Magnetic Sensing Platform

To put the current monitoring technique previously proposed in [21] into practice, we designed the hardware platform depicted in Fig. 9(a). Four MR sensors (HMC2003) were positioned orthogonally to each other in space, so as to measure the magnetic field around the cable surface by rotation. As mentioned above, a triple-layer magnetic shielding was employed for the sake of reducing interference from the environment (e.g., the Earth's magnetic field, magnetic fields generated from other nearby cables, and other background interferences). In order to suppress the intrinsic noise (e.g., *1/f* noise) of the MR sensors, magnetic flux concentrators (MFCs) made of Mu-metal were designed to strengthen signals and improve the signal-to-noise ratio. The 3D schematic diagram of the setup mounted around the power cable is shown in Fig. 9(b). The sensors and MFCs were fixed by plastic molding and attached to the inner side of the shielding so that the sensors could be moved to measure magnetic fields around the cable surface by rotating the shielding externally. Measurement data was acquired by a data acquisition card (*NI USB-6211*) programmed with LabVIEW, as shown in Fig. 9(c). A small hole in the triple-layer shielding enabled wires to connect the sensors with the power supply and the data acquisition (DAQ) card. The data was acquired, then processed through the stochastic algorithm to complete reconstruction. Details regarding each element of the setup are provided below.

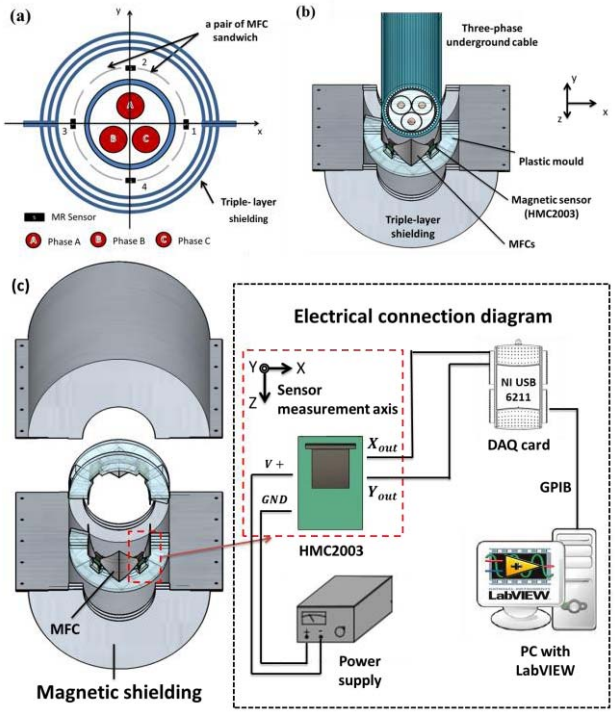

Fig. 9. Magnetic-field sensing platform for load current monitoring on the underground power cable. (a) Cross-sectional view of sensing and shielding components. (b) 3D schematic diagram of sensing component and its installation around the power cable. (c) Electrical connections for data acquisition and processing.

A. Magnetic Sensors

As mentioned in Section II(A), the 2-axis magnetic sensing (B_t and B_n) in a plane is needed for reconstructing the vector of the resultant magnetic field at any point on the cable surface. Majority of the commercial MR sensors in the market are 1- and 3-axis products [35], [36]. Thus, the off-the-shelf 3-axis sensors were used in the work. The permalloy-based Honeywell HMC2003 [36] is an integrated sensor capable of measuring magnetic fields in X-, Y- and Z- axis simultaneously. As described in Fig. 9(b), the sensor Z-axis is along the cable direction, which is useless in magnetic field measurement. However, the rest Y- and Z- axis are located in a plane to measure the non-uniform magnetic fields around the cable surface as illustrated in Fig. 2. The sensor has a measurement range of 2 gauss and a 40–μgauss resolution to measure low magnetic field strengths. Based on the FEM results in Section II(A), the RMS magnetic flux density around the cable surface is about 10 mG when the rated current of the cable is 1A. Therefore, the measurement range of 2 gauss is enough to measure a cable of rated current within 200 A. The compact-in-size sensor (19 $\times$25.4 mm^2) has an on-chip +2.5V voltage reference that operates from a single 6 to 15 V supply. The sensor array of our setup is composed of four HMC2003 sensors (Fig. 10(a)) [36]. These anisotropic magnetoresistance (AMR) sensors can be affected by the large transient magnetic field when exposed to the environment. For HMC 2003, a magnetic field stronger than 2 gauss can make the pre-set magnetization direction align to the exposed fields rather than the required easy axis directions, giving an

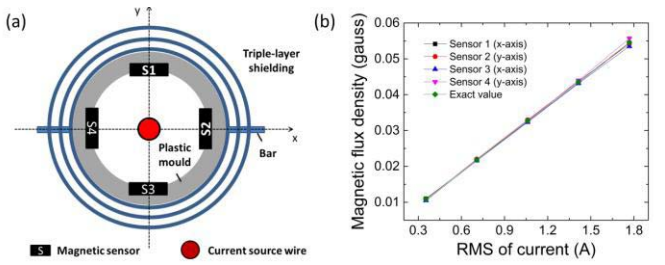

Fig. 10. Sensor calibration for consistent performance. (a) Experiment setup including MR sensors (HMC2003), AC current source at the center, and triple-layered shielding. (b) Response curves of sensors after reset. Exact magnetic flux density under various currents are calculated by Biot-Savart law.

erroneous measurement [37]. The HMC2003 has an on-chip current strap for re-magnetization, and uses a 3-4 amp pulse to reset the permalloy film of the sensors via magnetic switching technique before every measurement. In order to accurately observe the performance of four sensors, we installed an AC current source wire in the center of the shielding with equivalent distance (60mm) to all sensors (Fig. 10(a)). Sensor performances are consistent after reset, matching the exact values calculated by Biot-Savart law (Fig. 10(b)).

B. Magnetic Shielding

Magnetic shielding reduces environmental magnetic interference which can improve the accuracy of the reconstruction results. The interference can be both DC (e.g., the Earth's magnetic field) and AC (e.g., magnetic fields generated from other nearby cables) fields. To ensure a powerful attenuation ratio of the interference field, we designed a triple-layer magnetic shielding with a high permeability material (Mu-metal), as shown in Fig. 11(a). Mu-metal has a high relative permeability value (80,000–100,000) and is useful for shielding against DC and low-frequency AC magnetic fields. The shielding was designed with three thin layers instead of one thick layer in order to reduce cost and weight [38]. Each layer has a different radius but with a hole in the middle of the same radius to clamp the cable (Fig. 11(b)). The radius of inner layer was 30 mm distance away from the cable surface, and the FEM showed the round shielding has no effect on the original magnetic field distribution around the cable surface. The upper half and lower half of the shielding were separated so that an underground cable to be clamped in between by screwing the bolts at both sides. The shielding performance was various in DC and AC conditions [39], [40] and both were tested. In FEM simulation, the external DC magnetic field was set to be 10^{-4} Tesla and was attenuated to 6.63×10^{-10} Tesla inside the shielding. The results showed a satisfactory attenuation ratio [41] (incident magnetic field (H_0) over the transmitted field (H_i), H_0/H_i) of 1.5×10^5. The experimental AC testing at different frequencies was conducted where a uniform external AC magnetic field was generated by a pair of coils outside the shielding and the magnetic flux density was measured at the center inside the shielding. The magnitude of the external AC magnetic field were set at a weak value (0.1 gauss) and a strong value (4 gauss) to simulate various environment. As shown in Fig. 11(c), the attenuation ratio decreases as the frequency

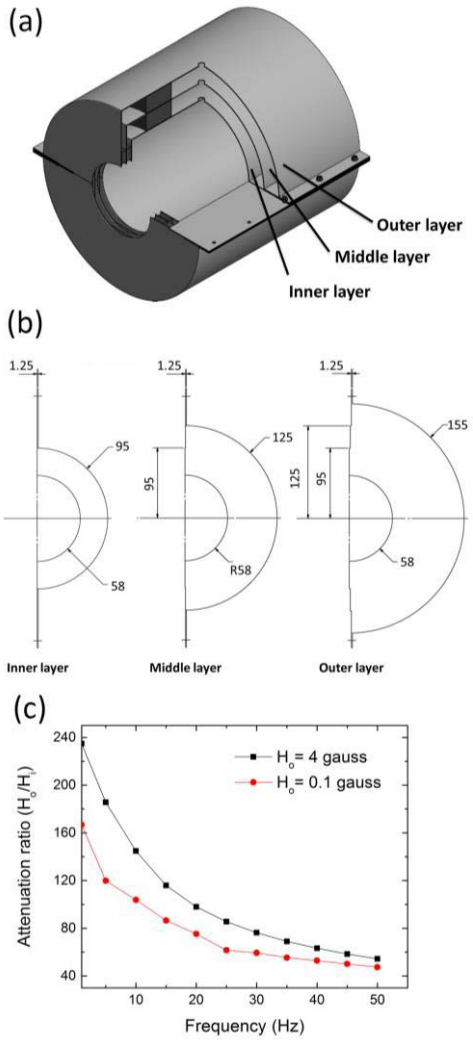

Fig. 11. Magnetic shielding design and test. (a) Triple-layer magnetic shielding made by Mu-metal. (b) Design parameters: thickness of each layer, 1.25 mm; outer radius of each layer: 95, 125 and 155 mm; radius of the hole in the middle of each layer: 58 mm; overall length: 30 cm; weight, 3 kg. (c) Attenuation ratio (H_0/H_i) at various exposed magnitude (0.1 and 4 gauss) and frequency (0 to 50 Hz) of the external magnetic field.

increases. The results also show that the attenuation ratio is increased when the magnitude of the external field is stronger (the stronger magnetic field leads to a larger permeability of shielding when not saturated, and thus improving the attenuation ratio at low frequency) [42]. The external AC field strength is attenuated by a factor of 50 at 50 Hz, indicating that the shielding can effectively protect the on-site measurement from the magnetic interferences generated by the nearby underground power cables working at mains frequency (50 Hz).

C. Magnetic Flux Concentrators (MFCs)

MFCs with high magnetic permeability collect magnetic flux lines and lead to a magnetic field amplification in the sensing gap so as to improve signal-to-noise ratios. As such, the homogeneous Mu-metal ($\mu_r \approx 10^4 \sim 10^5$) was used because its permeability is higher than other typically used magnetic material like ferrite ($\mu_r \approx 10^3 \sim 10^4$).

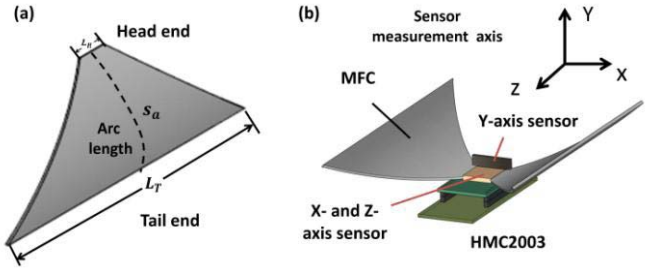

Fig. 12. MFC design. (a) Curved trapezoidal MFC. (b) HMC2003 sensor sandwiched by a pair of curved trapezoidal MFCs.

The trapezoidal MFC structure was adopted for providing a larger amplification ratio than the common bar-shaped ones [43]. The trapezoidal MFCs were made into a curved shape which conforms to the cylindrical geometry of cable and shielding in order to be installed into the small confined space inside the magnetic shielding as shown in Fig. 12(a). The amplification ratio can be improved by increasing the MFC arc length (S_a), and the length ratio of the tail end (L_T) to the head end (L_H) [44]. To achieve a long arc length, the four pairs of MFCs together with the four MR sensors formed a circular arrangement. A large length ratio of the tail end (L_T) to the head end (L_H) can be realized by minimizing the length of head end and increasing the length of tail end. The length of MFC's head end was minimized to 10 mm, which was equal to the width of the X-axis sensor for X-axis measurement (Fig. 12(b)). The tail end of MFC was 100 mm, which was ten times the head end. The amplification ratio decreases when the thickness of the MFC increases [44]. Therefore, the MFC thickness was designed with 1 mm which is the minimum thickness provided by the manufacturer, reducing the shielding weight at the same time.

IV. Onsite Experiment

The on-site experiment to test the developed platform was conducted in a substation. The substation is equipped with remote terminal units (RTUs) and a supervisory control and data acquisition (SCADA) system. The 60 MVA transformers in the substation bridge the transmission and distribution network by stepping down the voltage from 275 kV or 132 kV to 22 kV or 11 kV, then transmit power to the demand side through the BS6622 three-phase three-core armored XLPE stranded underground power cables. These underground cables are typically buried underground outside the substation. They are only exposed in the cable room in the substation where our developed platform can be installed onto one of the cables for testing.

Prior to the actual measurement, the shielding performance was validated. The magnetic flux density measured by the gauss meter (DT-1130 manufactured by PWOW®) in the background of the cable room was 0.61 μT (Fig. 13(a)). The reading dropped to 0.00 μT (Fig. 13(b)) when the gauss meter was placed inside the shielding, showing that the shielding can effectively suppress the external interference.

The layout of the BS6622 power cables in the cable room is shown in Fig. 14(a). Though the underground power cables are installed in close proximity to each other, the influence of

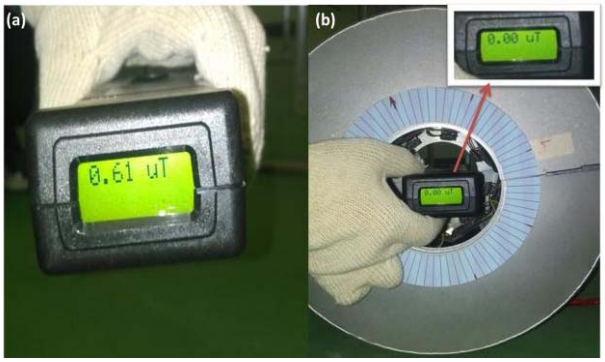

Fig. 13. Shielding function verification. (a) Magnetic flux density measured without shielding. (b) Magnetic flux density measured with shielding.

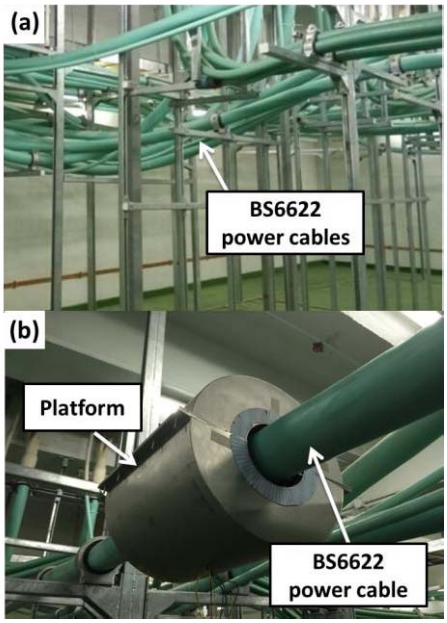

Fig. 14. Experiment to measure magnetic fields around underground power cable in the cable room of a zone substation. (a) Complicated placement of underground power cables at the substation. (b) Sensing platform installed on the underground power cable.

the induced currents by neighboring cables on the target cable is negligible compared to the load currents according to the results in Section II. As shown in Fig. 14(b), the platform was installed on the target BS6622 power cable. The sensor array composing of four sensors was rotated in the step of 10° anti-clockwise in a full cycle to capture the RMS magnetic fields around the cable surface.

The magnetic flux density measured by X- and Y- axis sensor are shown in Fig. 15, respectively. The RMS value of magnetic flux density repeats at intervals of about 2/3 π with three crests and troughs, which is consistent with the previous analysis. Magnetic flux density was amplified by about 4.18 times by the MFCs, as shown in Fig. 15(a). For the Y-axis sensor, the measured results with and without MFCs were more or less the same, as it is not sandwiched by MFCs (Fig. 15(b)). The measured magnetic flux densities by X- and Y- axis sensor around the cable surface at 10° interval were then processed to reconstruct the three-phase current sources.

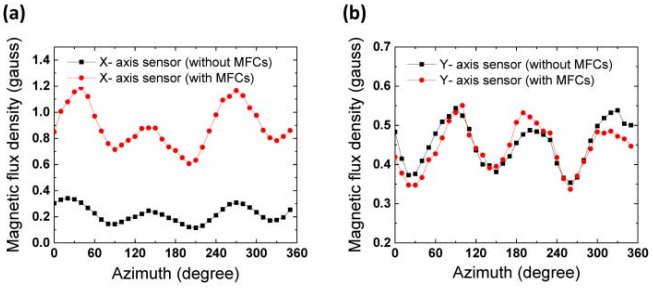

Fig. 15. Measured RMS magnetic flux density around the cable surface. (a) Measured signal by the X-axis sensor with and without MFCs. (b) Measured signal by the Y-axis sensor with and without MFCs.

TABLE II

RECONSTRUCTED PHASE CONDUCTOR POSITIONS OF UNDERGROUND POWER CABLE

Reconstruction No.	Phase A	Phase B	Phase C
	(x, y) (cm)	(x, y) (cm)	(x, y) (cm)
1	(2.57, 0.94)	(-1.54,1.29)	(0, -2.45)
2	(2.54, 0.92)	(-1.56, 1.31)	(0, -2.56)
3	(2.61, 0.95)	(-1.60, 1.34)	(0, -2.64)
4	(2.68, 0.98)	(-1.60, 1.37)	(0, -2.49)
5	(2.54, 0.92)	(-1.56, 1.31)	(0, -2.56)

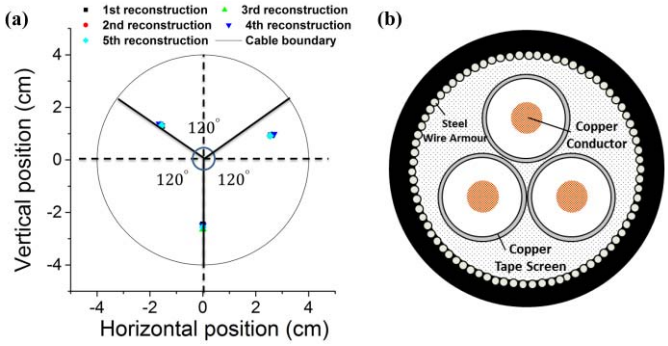

Fig. 16. Reconstructed phase conductor positions. (a) Reconstructed center point for each phase conductor position. (b) Cross-sectional view of BS6622 three-phase three-core armored 22 kV XLPE stranded underground power cable [25].

The reconstruction algorithm was repeated five times. Each group of the reconstructed three-phase three-core conductor positions is shown in Table II and plotted in Fig. 16(a). Though the stochastic optimization algorithm each time starts with a different initial position P_o, the reconstructed position results are very close among each execution. The reconstructed center points of phase conductor positions were almost at the middle between the origin and cable surface. The reconstructed physical positions of phase conductors were more or less symmetrical at 120° from each other. These two features conform to the standard BS6622 cable configuration [25] as shown in Fig. 16(b).

The reconstructed three-phase current values were 32.06, 32.95 and 35.87 A, respectively. During measurement, the

Fig. 17. Direct current reading from CTs in the gas insulated switchgear box.

TABLE III
MEASURED AND RECONSTRUCTED CURRENT VALUE FOR EACH PHASE OF UNDERGROUND POWER CABLE

	Time	Phase A (A)	Phase B (A)	Phase C (A)
Measured Current	12:03	32.50	33.75	35.00
	12:13	31.60	33.00	34.00
	12:23	31.75	32.50	34.50
	12:33	32.00	33.80	35.00
	12:43	33.60	34.00	37.00
	12:53	32.50	32.75	34.25
	Average	32.32	33.30	34.95
Reconstructed value		32.06	32.95	35.87
Relative error		0.8%	1.06%	2.6%

actual current values were recorded from a reading meter directly installed in the gas insulated switchgear box as shown in Fig. 17. The CT inside the box clamps the three-phase conductors of the target underground cable. Since the underground power cable being measured was connected to the demand side, the current in the cable varied slightly over time during the measurement as shown in Table III. The reconstructed current values closely matched with the average amplitudes of the recorded values (32.32, 33.3 and 34.95 A) from the meter. The largest relative error occurred at phase C (2.6%). In general, the reconstructed electrical and geometrical parameters agreed very well with the values measured by the CT.

In order to evaluate the effect of the induced current experimentally, the magnetic flux density around the cable surface was also measured when the cable was de-energized. The wire that connects the steel wire armor with the ground was disconnected to prevent the possible current flowing from the ground. Under this circumstance, the magnetic field generated should only come from the induced current. The result shows that the magnitude of the RMS magnetic flux density by

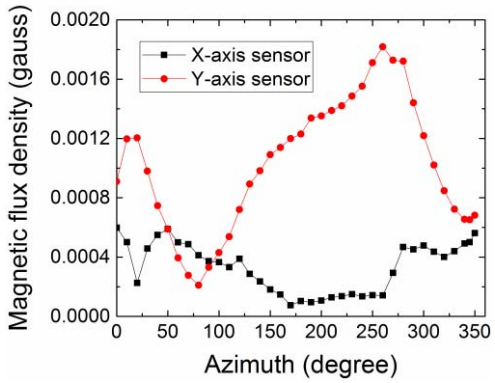

Fig. 18. Measured RMS magnetic flux density around the cable surface when the cable is de-energized.

the induced current ($\sim$ 0.001 gauss) was much smaller those measured in the current-energized status ($\sim$ 0.447 gauss), and there only exist two peaks and troughs of the magnetic flux density as measured by X- and Y- axis sensor (Fig. 18). The reason for the two rather than three peaks and troughs is because the induced currents in the three phase conductors of the target cable are imbalanced as they experienced different magnetic field. As mentioned in Section II(A), the RMS value of the magnetic flux density around the cable surface is about 0.01 gauss when the rated currents on phase conductors are 1 A. Therefore, the magnitude of induced current should be around 0.1 A as the magnitude of the magnetic flux density measured was about 0.001 gauss. This result verified our simulation result in Section II, which shows that the induced current is much smaller than the load currents ($\sim$ 30 A) and thus negligible.

The platform has been verified to reconstruct currents of a 22 kV underground power cable without galvanic connection with the primary circuit successfully, which is highly beneficial to safety. The sensing elements, MR sensors, are supplied with a low voltage, and avoid any overheating like CTs. The whole platform is compact in size ($\sim$0.02 m^3) and low-cost in contrast to CTs by using commercially available MR sensors. Apart from these characteristic, the platform is also envisioned to improve sensing capability on current amplitude and frequency potentially. Currently, CTs cannot detect large currents due to core saturation, and their frequency bandwidth are restricted from tens to several kHz [45]. The developed platform is a non-contact measurement method which exploits the magnetic fields to reconstruct the currents. From this work, it can be seen that the magnetic field around the cable surface is only several tenths of a gauss when the rated current is around 30 A, which is well within the measurement range of the MR sensors. In fact, many MR sensors can provide a large range of measurement. For example, multilayered giant magnetoresistive sensors (GMRs) made by NVE company (AA, AB, and AD product prefixes) show an approximate 30 gauss saturation field [46]. Therefore, the upper measurement range of the current can be as large as thousands of amperes, making it possible to detect large current blips occurred in the early stages of cable failure (hundreds of amperes). In addition, MR sensors also provide a wider

frequency bandwidth from DC to MHz (e.g., 1 MHz upper-frequency limit of GF708 sensors manufactured by Sensitec [35]). A wider frequency bandwidth (possibly from DC to MHz) is necessary for monitoring high-voltage DC transmission grids or high-frequency electromagnetic pulses (MHz) of an incipient fault within an underground power cable (*e.g.,* partial discharge between the sheath and conductor [47]).

V. Conclusion

In this study, we developed a non-invasive magnetic-field-sensing-based platform for monitoring the loading current of multi-core underground power cables. The currents were calculated by an iterative inverse algorithm with stochastic optimization to minimize the Euclidean difference of the magnetic field distribution between the calculated and the measured in our algorithm. The method is of high accuracy after evaluating the effect of the leakage and induced currents flowing on the multi-core underground power cable. A triple-layer shielding was designed to reduce the effect of external interference, and was proven to provide an attenuation ratio of 10^5 for DC field and 50 for AC field at 50 Hz. MFCs were also designed and implemented to improve the signal-to-noise ratio, and were proven to strengthen the magnetic field signal by 4.18 times. The platform was then tested in the cable room of a zone substation, and the reconstruction results closely match with the cable geometrical configuration and the current values of the cable measured by the CT. By employing our developed platform, the non-invasive current monitoring of underground power cables was effectively realized. The sensing elements are MR sensors, which consume low power and there is no necessity of complex hardware maintenance. The device is also designed in a compact and low-cost way. The deployment of MR sensors is promising for enhancing measurement upper limit and frequency bandwidth compared to traditional CTs.

In future work, we plan to apply more sensors into the sensor array so that the measurement time can be reduced. By implementing signal processing and reconstruction calculation with an embedded system, this real-time monitoring technique can be realized with an even more compact and all-in-one standalone system for a large-scale deployment in the future Smart Grid.

Acknowledgment

The authors would like to thank the Hongkong Electric Company Limited, Hong Kong, for assisting the onsite experiment.

References

[1] A. Ametani, "A general formulation of impedance and admittance of cables," *IEEE Trans. Power App. Syst.*, vol. PAS-99, no. 3, pp. 902–910, May 1980.

[2] A. Ukil, H. Braendle, and P. Krippner, "Distributed temperature sensing: Review of technology and applications," *IEEE Sensors J.*, vol. 12, no. 5, pp. 885–892, May 2012.

[3] L. Marti, "Simulation of transients in underground cables with frequency-dependent modal transformation matrices," *IEEE Trans. Power Del.*, vol. 3, no. 3, pp. 1099–1110, Jul. 1988.

[4] J. P. Barton and D. G. Infield, "Energy storage and its use with intermittent renewable energy," *IEEE Trans. Energy Convers.*, vol. 19, no. 2, pp. 441–448, Jun. 2004.

[5] B. Singh, K. Al-Haddad, and A. Chandra, "A review of active filters for power quality improvement," *IEEE Trans. Ind. Electron.*, vol. 46, no. 5, pp. 960–971, Oct. 1999.

[6] D. A. Douglass and A. Edris, "Real-time monitoring and dynamic thermal rating of power transmission circuits," *IEEE Trans. Power Del.*, vol. 11, no. 3, pp. 1407–1418, Jul. 1996.

[7] A. B. L. Ribeiro, N. F. Eira, J. M. Sousa, P. T. Guerreiro, and J. R. Salcedo, "Multipoint fiber-optic hot-spot sensing network integrated into high power transformer for continuous monitoring," *IEEE Sensors J.*, vol. 8, no. 7, pp. 1264–1267, Jul. 2008.

[8] P. Ripka, K. Draxler, and R. Styblikova, "Measurement of DC currents in the power grid by current transformer," *IEEE Trans. Magn.*, vol. 49, no. 1, pp. 73–76, Jan. 2013.

[9] S. Ziegler, R. C. Woodward, H. H.-C. Iu, and L. J. Borle, "Current sensing techniques: A review," *IEEE Sensors J.*, vol. 9, no. 4, pp. 354–376, Apr. 2009.

[10] A. Papp and H. Harms, "Magnetooptical current transformer. 1: Principles," *Appl. Opt.*, vol. 19, no. 22, pp. 3729–3734, 1980.

[11] H. Harms and A. Papp, "Magnetooptical current transformer. 3: Measurements," *Appl. Opt.*, vol. 19, no. 22, pp. 3741–3745, 1980.

[12] H. Farhangi, "The path of the smart grid," *IEEE Power Energy Mag.*, vol. 8, no. 1, pp. 18–28, Jan./Feb. 2010.

[13] B. Lee, "Review of the present status of optical fiber sensors," *Opt. Fiber Technol.*, vol. 9, no. 2, pp. 57–79, 2003.

[14] G. Wild and S. Hinckley, "Acousto-ultrasonic optical fiber sensors: Overview and state-of-the-art," *IEEE Sensors J.*, vol. 8, no. 7, pp. 1184–1193, Jul. 2008.

[15] H. Sun *et al.*, "All-dielectric electrooptic sensor based on a polymer microresonator coupled side-polished optical fiber," *IEEE Sensors J.*, vol. 7, no. 4, pp. 515–524, Apr. 2007.

[16] J. Lenz and A. S. Edelstein, "Magnetic sensors and their applications," *IEEE Sensors J.*, vol. 6, no. 3, pp. 631–649, Jun. 2006.

[17] P. Orr *et al.*, "An optically-interrogated Rogowski coil for passive, multiplexable current measurement," *IEEE Sensors J.*, vol. 13, no. 6, pp. 2053–2054, Jun. 2013.

[18] Y. Liu, F. Lin, Q. Zhang, and H. Zhong, "Design and construction of a Rogowski coil for measuring wide pulsed current," *IEEE Sensors J.*, vol. 11, no. 1, pp. 123–130, Jan. 2011.

[19] P. Ripka, "Electric current sensors: A review," *Meas. Sci. Technol.*, vol. 21, no. 11, p. 112001, 2010.

[20] R. H. Bhuiyan, R. A. Dougal, and M. Ali, "Proximity coupled interdigitated sensors to detect insulation damage in power system cables," *IEEE Sensors J.*, vol. 7, no. 12, pp. 1589–1596, Dec. 2007.

[21] X. Sun *et al.*, "Operation-state monitoring and energization-status identification for underground power cables by magnetic field sensing," *IEEE Sensors J.*, vol. 13, no. 11, pp. 4527–4533, Nov. 2013.

[22] I. Paprotny, Q. Xu, W. W. Chan, R. M. White, and P. K. Wright, "Electromechanical energy scavenging from current-carrying conductors," *IEEE Sensors J.*, vol. 13, no. 1, pp. 190–201, Jan. 2013.

[23] D. E. Thomas, E. M. Wiggins, T. M. Salas, F. S. Nickle, and S. E. Wright, "Induced transients in substation cables: Measurements and models," *IEEE Trans. Power Del.*, vol. 9, no. 4, pp. 1861–1868, Oct. 1994.

[24] J. E. Lenz, "A review of magnetic sensors," *Proc. IEEE*, vol. 78, no. 6, pp. 973–989, Jun. 1990.

[25] Derrick. (2016). *BS6622/BS7835 Three Core Armoured 22kV XLPE Stranded Copper Conductors*, accessed on May 18, 2016. [Online]. Available: http://uk.prysmiangroup.com/en/business_markets/markets/ti/datasheets/3_core_arm_22kv_ccBS662BS7835.pdf

[26] D. S. Freitas, A. T. Prata, and A. J. D. Lima, "Thermal performance of underground power cables with constant and cyclic currents in presence of moisture migration in the surrounding soil," *IEEE Trans. Power Del.*, vol. 11, no. 3, pp. 1159–1170, Jul. 1996.

[27] J. Hegyi and A. Y. Klestoff, "Current-carrying capability for industrial underground cable installations," *IEEE Trans. Ind. Appl.*, vol. 24, no. 1, pp. 99–105, Jan. 1988.

[28] G. Bahder, C. Katz, J. Lawson, and W. Vahlstrom, "Electrical and electro-chemical treeing effect in polyethylene and crosslinked polyethylene cables," *IEEE Trans. Power App. Syst.*, vol. PAS-93, no. 3, pp. 977–989, May 1974.

[29] S. Konglysan and W. Rungseevijitprapa, "XLPE insulated high voltage underground cable assessment of leakage current studies," *J. Comput. Commun. Instrum. Eng.*, vol. 2, no. 2, pp. 162–164, 2015.

[30] A. N. Guven and S. A. Sebo, "Analysis of ground fault curreni distribuiion along underground cables," *IEEE Trans. Power Del.*, vol. 1, no. 4, pp. 9–18, Oct. 1986.

[31] H. Oonishi, F. Urano, T. Mochizuki, K. Soma, K. Kotani, and K. Kamio, "Development of new diagnostic method for hot-line XLPE cables with water trees," *IEEE Trans. Power Del.*, vol. 2, no. 1, pp. 1–7, Jan. 1987.
[32] A. A. Khan, N. Malik, A. Al-Arainy, and S. Alghuwainem, "A review of condition monitoring of underground power cables," in *Proc. Int. Conf. Condition Monitor. Diagnosis (CMD)*, Sep. 2012, pp. 909–912.
[33] P. G. Alotto *et al.*, "Stochastic algorithms in electromagnetic optimization," *IEEE Trans. Magn.*, vol. 34, no. 5, pp. 3674–3684, Sep. 1998.
[34] A. Canova, F. Freschi, M. Repetto, and M. Tartaglia, "Description of power lines by equivalent source system," *Int. J. Comput. Math. Elect. Electron. Eng.*, vol. 24, no. 3, pp. 893–905, 2005.
[35] SENSITEC. (2015). *GF708: Magnetoresistive Magnetic Field Sensor*, accessed on May 18, 2016. [Online]. Available: http://www.sensitec.com/lp/
[36] Honeywell. (2011). *3-Axis Magnetic Sensor Hybrid HMC2003*, accessed on May 18, 2016. [Online]. Available: https://physics.ucsd.edu/neurophysics/Manuals/Honeywell/HMC_2003.pdf
[37] Honeywell. (2008). *Set/Reset Function for Magnetic Sensors*, accessed on Jan. 6, 2017. [Online]. Available: http://www.seraphim.com.tw/upfiles/c_supports01284968029.pdf
[38] R. B. Schulz, V. C. Plantz, and D. R. Brush, "Shielding theory and practice," *IEEE Trans. Electromagn. Compat.*, vol. 30, no. 3, pp. 187–201, Aug. 1988.
[39] T. Cavallin, R. Quarantiello, A. Matrone, and G. Giunchi, "Magnetic shielding of MgB_2 tubes in applied DC and AC field," *J. Phys.*, vol. 43, no. 1, pp. 1015–1018, 2006.
[40] H. Waki, H. Igarashi, and T. Honma, "Analysis of magnetic shielding effect of layered shields based on homogenization," *IEEE Trans. Magn.*, vol. 42, no. 4, pp. 847–850, Apr. 2006.
[41] J. F. Hoburg, "Principles of quasistatic magnetic shielding with cylindrical and spherical shields," *IEEE Trans. Electromagn. Compat.*, vol. 37, no. 4, pp. 574–579, Nov. 1995.
[42] M. Reta-Hernández and G. G. Karady, "Attenuation of low frequency magnetic fields using active shielding," *Electr. Power Syst. Res.*, vol. 45, no. 1, pp. 57–63, Apr. 1998.
[43] X. Sun, L. Jiang, and P. W. T. Pong, "Magnetic flux concentration at micrometer scale," *Microelectron. Eng.*, vol. 111, pp. 77–81, Nov. 2013.
[44] K. Zhu and P. W. T. Pong, "Curved trapezoidal magnetic flux concentrator design for improving sensitivity of magnetic sensor in multiconductor current measurement," in *Proc. 5th Int. Symp. Next-Generat. Electron. (ISNE)*, May 2016, pp. 1–2.
[45] D. A. Douglass, "Current transformer accuracy with asymmetric and high frequency fault currents," *IEEE Trans. Power App. Syst.*, vol. PAS-100, no. 3, pp. 1006–1012, Mar. 1981.
[46] NVE Corporation. (2016). *Leaders in Practical Spintronics*, accessed on May 18, 2016. [Online]. Available: http://www.nve.com/
[47] Y. Tian, P. L. Lewin, and A. E. Davies, "Comparison of on-line partial discharge detection methods for HV cable joints," *IEEE Trans. Dielectr. Electr. Insul.*, vol. 9, no. 4, pp. 604–615, Aug. 2002.

Ke Zhu (S'12) received the B.E. degree in electrical engineering from China Three Gorges University, Yichang, China, in 2013. He is currently pursuing the Ph.D. degree in electrical and electronic engineering with the University of Hong Kong. His current research and academic interests focus on computational electromagnetics, electric power transmission monitoring, and the application of magnetoresistive sensors in smart grid.

Wei Han (S'16) received the B.Eng. degree from Northeastern University, Shenyang, China, in 2014, and the M.Eng. degree from the University of Hong Kong, Hong Kong, China, in 2015, where he is currently pursuing the Ph.D. degree with the Department of Electrical and Electronic Engineering. His research interests include wireless power transfer techniques, power electronics, and renewable energies.

Wing Kin Lee received the B.Sc. degree and the M.Sc. degree from the University of Hong Kong, in 1976 and 1988, respectively, and the M.B.A. degree from the Chinese University of Hong Kong in 1990. He earned industrial experience while involved with power and communication utility companies in Hong Kong. He is a professional in electrical services and power engineering, and currently as a Senior Teaching Consultant with the University of Hong Kong. His current research interests include smart grid demand side management, electrical load signature, and vertical transportation.

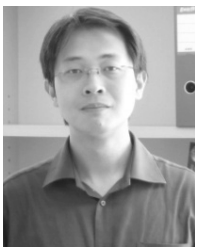

Philip W. T. Pong (SM'13) received the Ph.D. degree in engineering from the University of Cambridge in 2005. He was a Post-Doctoral Researcher with the Magnetic Materials Group, National Institute of Standards and Technology for three years. He is a Physicist and an Electrical Engineer working on magnetoresistive magnetic field sensors and smart grid with the Department of Electrical and Electronic Engineering, University of Hong Kong (HKU). In 2008, he joined the HKU Engineering Faculty as an Assistant Professor working on tunneling magnetoresistance sensors, and the application of magnetoresistive sensors in smart grid.